

Engineering spectro-temporal light states with physics-trained deep learning

Shilong Liu^{1,2,*}, Stéphane Virally¹, Gabriel Demontigny¹, Patrick Cusson¹, and Denis V. Seletskiy^{1,+}

¹femtoQ Lab, Department of Engineering Physics, Polytechnique Montréal, Montréal, Québec H3T 1J4, Canada

²Temp Optics, Montréal, Québec H3T 1W9, Canada

*corresponding dr.shilongliu@gmail.com

+corresponding denis.seletskiy@polymtl.ca

ABSTRACT

Frequency synthesis and spectro-temporal control of optical wave packets are central to ultrafast science, with supercontinuum (SC) generation standing as one remarkable example. Through passive manipulation, femtosecond (fs) pulses from nJ-level lasers can be transformed into octave-spanning spectra, supporting few-cycle pulse outputs when coupled with external pulse compressors. While strategies such as machine learning have been applied to control the SC's central wavelength and bandwidth, their success has been limited by the nonlinearities and strong sensitivity to measurement noise. Here, we propose and demonstrate how physics-trained convolutional neural network (P-CNN) can circumvent such challenges, showing few-fold speedups over the direct approaches. We highlight three key advancements enabled by the P-CNN approach: (i) on-demand control over spectral features of SC, (ii) direct generation of sub-3-cycle pulses from the highly nonlinear fiber, and (iii) the production of high-order solitons, capturing distinct "breather" dynamics in both spectral and temporal domains. This approach heralds a new era of arbitrary spectro-temporal state engineering, with transformative implications for ultrafast and quantum science.

Introduction

Supercontinuum (SC) generation arises from the intricate interplay of third-order and higher-order nonlinear optical processes when an ultrashort pulse propagates through a dispersive medium. Femtosecond (fs) laser oscillators delivering pulses with energies in the nanojoule (nJ) range can drive SC generation in highly nonlinear media such as photonic-crystal fibers or bulk-glass fibers¹⁻⁵. The resulting SC significantly broadens the input pulse's spectrum, creating a continuous, octave-spanning spectral band. With high brightness and exceptional spectral coverage, SC sources have become indispensable resources for applications including spectroscopy⁶, advanced microscopy^{7,8}, and optical coherence tomography^{9,10}. In ultrafast photonics, SC serves as a cornerstone for breakthroughs in ultrashort laser sources, including self-referenced¹¹ and offset-free^{12,13} frequency combs, generation of few- and single-cycle pulses¹⁴⁻¹⁶, and high-harmonic generation as well as attosecond pulse^{17,18}.

The precise manipulation of supercontinuum (SC) spectra is highly desirable but poses significant experimental challenges. This difficulty arises from the extreme sensitivity of SC generation to high-order dispersion and input pulse parameters, which drive a cascade of nonlinear interactions, including self- and cross-phase modulation (SPM and XPM), four-wave mixing (FWM), and Raman scattering. Commanding these processes to produce predictable SC outputs is formidable, requiring detailed characterization of linear dispersion, input pulse parameters, material dimensions, and third-order nonlinear coefficients^{3,5,19}. Achieving such control could enable the routine generation of octave-spanning and other synthesized spectra, thereby democratizing access to few-cycle waveform shaping^{14,16}.

Various strategies have been developed to gain control over SC generation. One approach involves selecting materials or waveguides with favorable dispersion properties⁵ or tailoring the nonlinearity of the medium, for instance, by adjusting the pressure inside gas-filled hollow-core fibers²⁰⁻²². Other methods focus on modifying the input pulse characteristics, such as pulse duration²³, energy²⁴, and pulse number²⁵, to tune the SC spectral

properties^{4,26}. Incorporating optimization algorithms, particularly genetic algorithms (GA), has enabled dynamic control of SC features^{25,27–29}, though the iterative search process, typically takes several minutes.

Recent theoretical studies employing machine learning have shown promising capabilities in predicting the spectral and temporal characteristics of SC^{30–32}. The main advantage of machine learning algorithms, such as artificial neural networks (ANNs), is to reduce this search time dramatically, from minutes to mere seconds, by mapping the highly nonlinear system onto a regression task^{33–35}. Experimental investigations have also leveraged machine learning to analyze specific SC properties, particularly in identifying extreme events^{36,37}. These studies typically rely on data-driven models³⁸, using phase or intensity inputs to train neural networks.

Despite these advancements, SC generation presents a strongly under-determined problem due to the dramatic spectral broadening relative to the input pulse. For example, the spectral-temporal features of SC are highly sensitive to the input wave's spectral phase, which evolves intricately during nonlinear propagation. When small perturbations become comparable to the experimental noise (numerical instabilities) in the training datasets, the search for the true solution becomes compromised. Consequently, large and accurate training datasets are often required for adequate network convergence^{34,38}.

In this work, we introduce a physics-trained convolutional neural network (P-CNN) to model pulse propagation in highly nonlinear media. The term “physics-trained” refers to embedding a physical spectro-temporal correlation function, specifically the Wigner function, into the deep learning network instead of relying solely on data-driven models. The Wigner function represents wavepackets in the spectral and temporal (chronocyclic) domain, enabling the use of convolutional neural networks (CNNs) to efficiently filter out uncorrelated noise and thus to reduce sensitivity to phase variations and eliminate artifacts related to the carrier-envelope offset phase (CEP)³⁹. Combined with a real-time optimization strategy, the trained P-CNN allows precise control of spectral and temporal dynamics, potentially down to single-cycle pulses.

Experimentally, we validated the P-CNN's performance across a broad range of input conditions. For strong input pulses, we demonstrated on-demand control of SC generation, including precise tuning of the bandwidth and spectral position. In the temporal domain, we achieved pulse durations as short as 12 fs (2–3 optical cycles) with a nonlinear compression factor of over 70, eliminating the need for expensive pulse compression methods^{4,22}. For weaker input pulses, we showed the ability to generate high-order solitons and performed detailed spectro-temporal analyses of their dynamics. These results underscore the P-CNN's capability to advance spectro-temporal manipulation of SC generation.

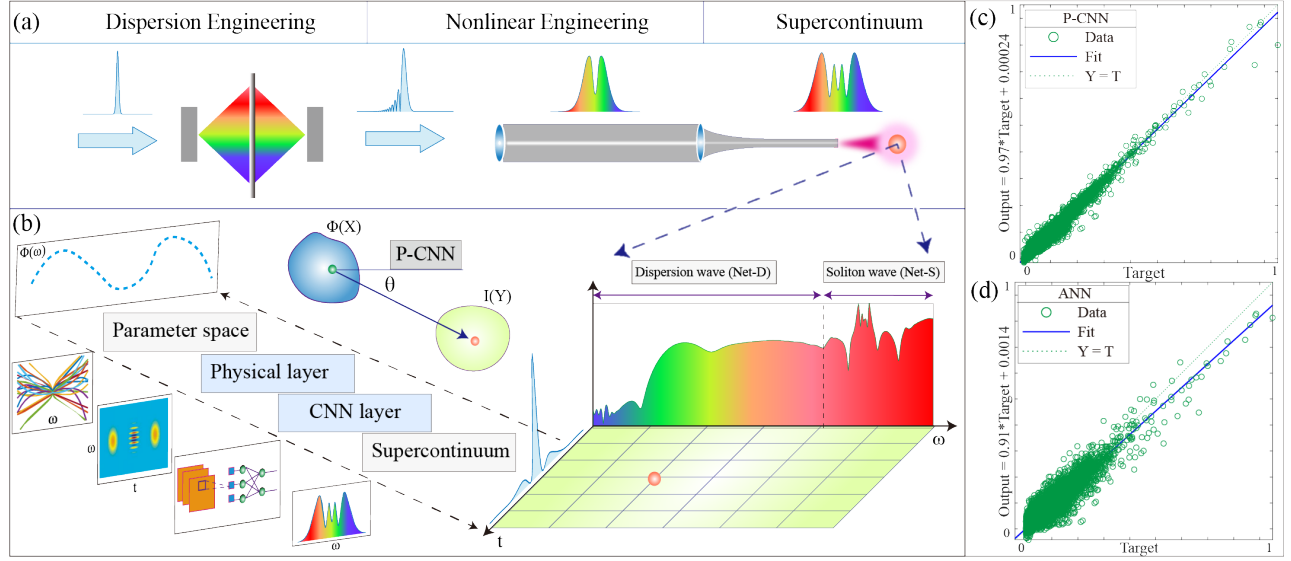


Figure 1. Experimental platform for spectro-temporal engineering assisted by a physics-trained convolutional neural network (P-CNN). (a) Schematized setup includes dispersion engineering, nonlinear engineering, and the supercontinuum generation stages. (b) The network architecture of P-CNN features the physical layer and CNN layer. Visualized spectro-temporal space of P-CNN output (right). (c)-(d) Regression comparison for the trained P-CNN and Artificial Neural Network (ANN).

P-CNN framework via the nonlinear optical platform

Figure 1 provides a comprehensive overview of the SC process and the architecture of the P-CNN. The optical setup consists of three primary sections. The first section, responsible for dispersion engineering (DE), includes a mode-locked fiber laser that generates femtosecond soliton pulses and a $4f$ pulse shaper, which enables precise control of dispersion. The output of the DE section feeds into the nonlinear engineering (NE) section, which comprises an Erbium-doped fiber amplifier (EDFA) and a highly nonlinear fiber (HNF) for supercontinuum generation. This setup allows for octave-spanning spectral broadening, unlocking advanced manipulation of SC outputs. For further details about the setup and simulations of SC generation, refer to **Methods-1: Setup and Simulations for Supercontinuum Generation**.

The dynamics of a laser pulse with a temporal envelope A propagating through the described setup can be modeled by a revised Generalized Nonlinear Schrödinger Equation (GNLSE)⁴:

$$\frac{\partial A}{\partial z} + \frac{\alpha}{2}A + \left[\sum_{\alpha=0}^2 \frac{iD_{\alpha}}{2} \left(\frac{-\partial^2}{\partial t^2} \right)^{\frac{\alpha}{2}} - \sum_{k \geq 2} \frac{i^{k+1} \beta_k}{k!} \frac{\partial^k}{\partial t^k} \right] A = i\gamma \left(1 + i\tau_{shock} \frac{\partial}{\partial t} \right) \left(A \int_{-\infty}^{+\infty} R(t') |A(z, t-t')|^2 dt' + i\Gamma_R(z, t) \right). \quad (1)$$

Here, the left-hand side of the equation models linear propagation effects, in which the third term represents fractional derivatives, while the fourth term describes regular higher-order derivatives. Both can be independently controlled using the $4f$ pulse shaper, where the fractional derivative introduces fractional dispersion (see, e.g., Refs. 40, 41). The right-hand side accounts for nonlinear effects. The Kerr coefficient γ governs the nonlinear refractive index, while $R(t)$ is the Raman response function. The term $\Gamma_R(z, t)$ captures the influence of spontaneous Raman noise. Additional nonlinear phenomena, such as self-steepening and optical shock formation, are characterized by a timescale $\tau_{shock} = \tau_0 = 1/\omega_0$.

Typically, the dynamics of SC generation are resolved through numerical simulations based on Eq. 1. However, such simulations are computationally intensive and highly sensitive to various parameters, including the energy and

spectro-temporal details of the realistic input pulse shape $A_{in}(t)$, which are often derived experimentally⁵. Machine learning algorithms present a promising alternative by simplifying this complex nonlinear system into a manageable linear representation. A convolutional neural network (CNN) can efficiently map the initial input field to the desired SC output parameters, expressed as:

$$I(Y) = \mathbb{P} - \text{CNN}_{\theta}[\Phi(X)], \quad (2)$$

where $\Phi(X)$ represents the spectral phase of the input field, and $I(Y)$ corresponds to the output parameters, such as spectral intensity $I(\omega)$ or temporal intensity $I(t)$. The P-CNN thus establishes a mapping between these parameter spaces via a nonlinear transformation θ , as illustrated in Fig. 1(b). The success of this mapping hinges on the CNN's ability to robustly identify optimal solutions despite the SC process's extreme sensitivity to input conditions.

The $\mathbb{P} - \text{CNN}$ framework integrates physical principles into a CNN, enabling robust determination of θ . The training process begins with Latin Hypercube Sampling (LHS)⁴² to scan the parameter space X_n and generate diverse random phase profiles $\Phi(\omega)$, in which X_n represents the dispersion distance (see **supplementary -2** for details). To address the sensitivity of direct training on such profiles³⁹, we reconstruct the pulse field $A_{in}(t)$ using complex spectral amplitude data retrieved from a Second-Harmonic-Generation Frequency-Resolved Optical Gating (SHG-FROG) setup. The Wigner function, which represents the pulse in the chronocyclic domain⁴³, is then calculated:

$$W(t, \omega) = \int_{-\infty}^{\infty} A\left(t + \frac{t'}{2}\right) A^*\left(t - \frac{t'}{2}\right) \exp(i\omega t') dt'. \quad (3)$$

This transformation ensures a self-consistent representation of the pulse in both the time and frequency domains, as depicted in the 'Physical Layer' of Fig. 1(b). The Wigner function is then fed into the CNN for training, with further details provided in **Methods-2: The Structure and Performance of Deep Learning Neural Networks**. The physics-trained network not only embeds spectro-temporal correlations into the model but also transforms the nonlinear SC generation problem into a network presentation. This enables the efficient identification of inverse solutions for the desired SC state.

We validated the performance of the trained P-CNN through simulations based on the GNLSE described in Eq. 1. Figure 1(c) shows a linear regression analysis comparing the target SC, yielding a correlation factor $R = 0.97$ for the fitting line. For comparison, using the same input data, we trained an artificial neural network (ANN) with three hidden layers containing 200, 200, and 100 neurons, respectively, commonly used for SC simulations^{34,35}. The regression results, shown in Fig. 1(d), yield a correlation factor of $R \approx 0.91$. By interpreting $(1 - R)$ as the fraction of uncompensated spectral correlations, the P-CNN demonstrates superior performance with a threefold reduction in sensitivity to nonlinear phase variations compared to the ANN. This improvement underscores the robustness of the physics-trained deep learning framework, forecasting significant speedups in achieving various target functions.

To implement these methods experimentally, we constructed two distinct P-CNN networks: "Network-Soliton" (Net-S) and "Network-Dispersive" (Net-D), as illustrated in Fig. 1(b). These networks are designed to handle different pulse energy regimes. For pulse energies $\lesssim 2$ nJ, the EDFA facilitates nonlinear spectral broadening through SPM, as shown in Fig. 1(a). This regime operates in the anomalous dispersion domain, leading to spectral sidelobe generation and soliton formation. For higher pulse energies, a cascade of EDFA and HNF generates SC characterized by an ultra-broadband dispersive wave, blueshifted into the normal dispersion regime.

Spectral Domain Engineering: Dispersive Wave

Both simulations and experiments indicate that the trained P-CNN can efficiently optimize $\Phi(\omega)$ to achieve virtually any physical target function. To further enhance performance, a real-time gradient descent search algorithm was implemented within the optical fiber system, utilizing the optimized solutions (see **Supplementary - 2** for details).

We first examine the controlled energy transfer from the soliton region (Net-S) to the dispersive wave (DW) region (Net-D). The Net-D region spans 1000–1430 nm, while the Net-S region covers 1430–1700 nm, constrained

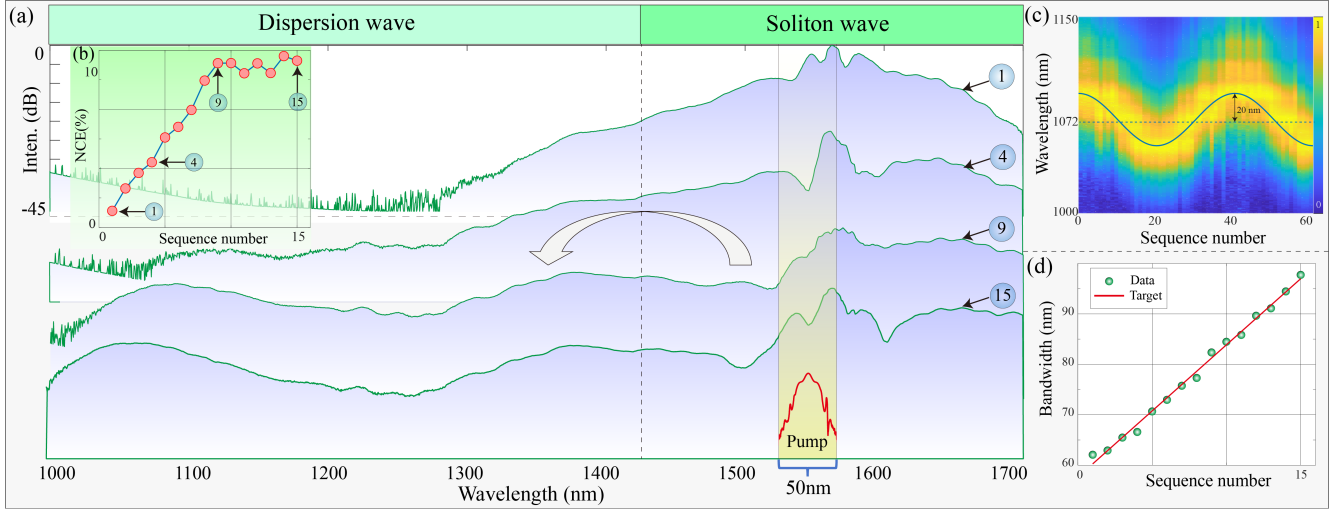


Figure 2. Spectral control of the supercontinuum. (a) Evolution of the SC spectra as a function of the input phase, controlled by the 4f shaper. (b) Calculated nonlinear conversion efficiency defined in Eq. 4 quantifying energy transfer from the soliton (Net-S) to dispersive wave (Net-D) spectral regions. The P-CNN enables engineering of the dispersive wave parameters: (c) The center wavelength oscillation with a target 3.7% modulation around 1070 nm and (d) linear tunability in bandwidth for DW.

by the optical spectrum analyzer's (OSA) range. Figure 2(a) shows the measured dependence of the SC output on the input spectral phase in log-linear scaling. Starting with modest broadening dominated by SPM (curve 1), P-CNN-assisted phase optimization progressively redistributes energy from soliton to dispersive wave (curves 4, 9, and 15). This process is quantified using the nonlinear conversion efficiency (NCE):

$$\eta_{NCE} = \frac{S_d}{S_d + S_s} \in [0, 1], \quad (4)$$

where $S_{d,s} = \int_{d,s} I(\lambda) d\lambda$ represents the integrated spectral energy over the respective spectral regions. An η_{NCE} of 1 indicates complete energy transfer to dispersive wave, while 0 signifies no transfer. Figure 2(b) depicts the measured NCE, showing linear growth followed by oscillations, with a maximum conversion of 12%. In the high-NCE, we examine the DW centered around ~ 1070 nm, which forms due to nonlinear interactions in the normal dispersion regime.

Next, we demonstrate the P-CNN's ability to achieve several features of DW, focusing on the center wavelength and bandwidth. The central wavelength, λ_{DS} , is defined by:

$$\lambda_{DS} = \lambda_0 + \Delta\lambda \cos(\Theta), \quad (5)$$

where λ_0 is the baseline wavelength, $\Delta\lambda$ is the modulation amplitude, and Θ is the angular coordinate. Figure 2(c) shows excellent agreement between the target modulation (solid blue line, $\Delta\lambda = 20$ nm, $\lambda_0 = 1070$ nm) and measured data, achieving a 3.7% modulation of the DW center wavelength.

We also demonstrate bandwidth manipulation with the DW center wavelength clamped at 1070 nm. The measured bandwidth closely follows the target range of 60-100 nm, as shown in Fig. 2(d). These combined results demonstrate the feasibility of a full engineering of the spectral density of the DW, while also tracing out a path toward an elegant control over the DW few-cycle temporal wavepacket.

Temporal Domain Engineering: Few-cycle Pulse

The dispersive wave (DW) is a powerful resources to generate short-wavelength laser pulses^{2,44}, and the flexibility demonstrated in the previous section highlights its potential for precise control of center wavelength and bandwidth.

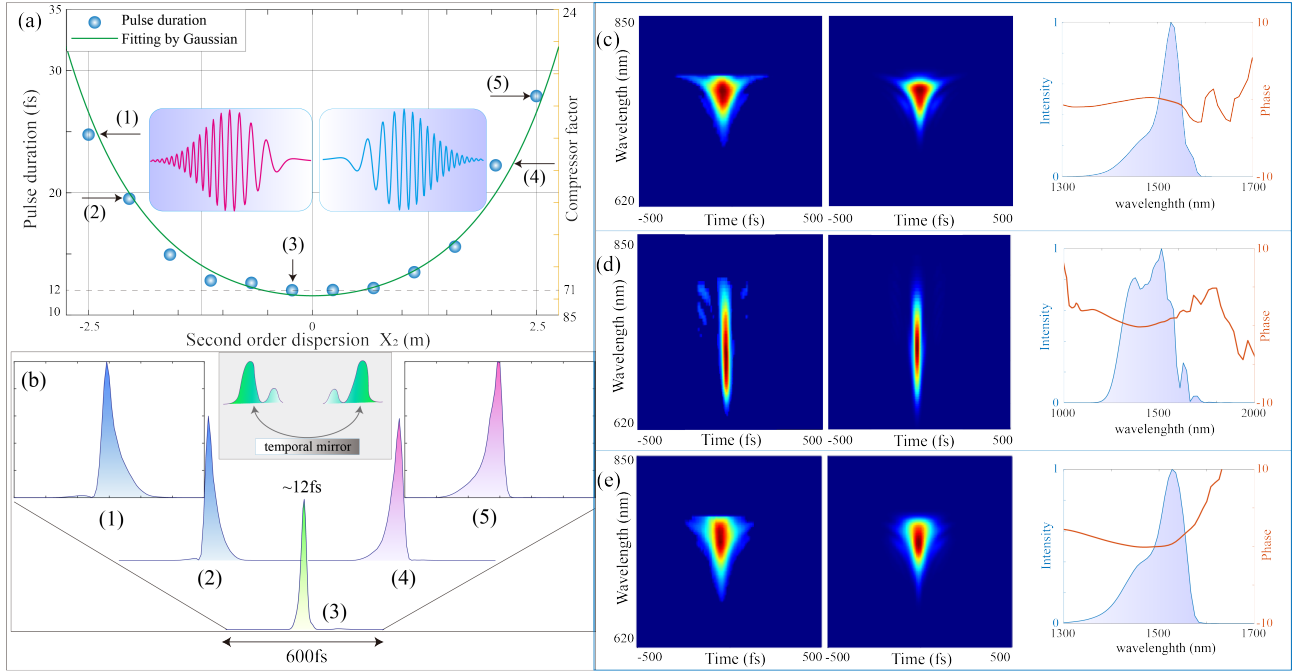


Figure 3. Temporal pulse duration engineering. (a) Ordinates the measured relationship between the pulse duration (left ordinate axis) and second-order dispersion distance (X_2), with the right axis displaying the nonlinear compression factor. (b) The reconstructed temporal intensity at five positions marked in (a). (c)-(e) The measured and reconstructed FROG traces for positions (1), (3), and (5) as indicated in panel (a), where the reconstructed spectral amplitude and phase are provided in the corresponding right-side panels.

The flattened and broad spectral feature observed in Fig. 2(a) further indicates the possibility of preparing ultrashort laser pulses. To isolate the DW from the long-wavelength spectral components of the Net-S band, we first employ a short-pass filter with a 1450 nm cutoff. Conventionally, this isolated DW is passed through dispersion-compensating elements, such as prism compressors or chirped mirrors, to produce near-transform-limited pulses. Instead, we leverage the P-CNN to simultaneously optimize the broadband DW generation and its compression, eliminating the need for additional compensators.

To evaluate the resulting pulse duration and profiles, second-harmonic FROG measurements are performed. The P-CNN is tasked to minimize the pulse duration, directly recognized through its Wigner-function-based training. For the optimized phase, the measured pulse duration is approximately 12 fs, corresponding to a compression factor of over 70, referenced as the initial pulse length 850 fs. To explore temporal compression dynamics, the second-order dispersion (X_2) is systematically adjusted. Fig. 3(a) shows the measured pulse durations as X_2 varies from -2.5 to 2.5 m, with a Gaussian scaling behavior (solid green line) reflecting symmetric temporal compression consistent with the largely symmetric spectral distribution of the DW.

The evolution of temporal profiles retrieved from FROG measurements is shown in Fig. 3(b). The data reveal preserved inversion symmetry in the wavepacket envelope ($X_2 \leftrightarrow -X_2$) and opposite orientations of pulse tails for the same $|X_2|$, reminiscent of a "temporal mirror" effect⁴⁵. This symmetry, supported by GNLSSE simulations (**Supplementary-4**), underscores the ability to shape temporal profiles through phase optimization.

Figures 3(c)-(e) present the measured and reconstructed FROG traces at positions (1), (3), and (5) from Fig. 3(a) and (b), alongside the corresponding reconstructed spectral amplitude and phase profiles. Notably, the spectral phase for positions (1) and (5) is opposite, resulting in symmetric structures in the temporal profiles. For positive and negative dispersion, symmetric self-steepening of the pulse is observed, where a steeper trailing edge implies enhanced spectral broadening via fiber nonlinearity and dispersion, facilitating the preparation of asymmetric few-cycle laser pulses⁴⁶.

Further analysis reveals the influence of higher-order dispersion, such as fourth-order dispersion, on pulse duration symmetry. For the shortest pulse duration of ~ 12 fs (Fig. 3(d)), the reconstructed spectral phase exhibits a residual second-order contribution near the central wavelength, corresponding to a group delay dispersion (GDD) of ~ 100 fs²- primarily arising from additional GDD in the setups of FROG that is estimated at around 120 fs². By flattening the spectral phase, a transform-limited pulse duration of 8.5 fs is achieved. This small systematic offset can be mitigated by optimizing the dispersion in the FROG setup. Additional details on the FROG setup are provided in **Supplementary-5**.

Spectro-Temporal Engineering: High-Order Solitons

In this section, we demonstrate the capability of the P-CNN to perform nonlinear pulse shaping in both the spectral and temporal domains. Here, the focus shifts back to the soliton Net-S region, previously defined. This task is particularly challenging due to the overlap between the pump spectrum and the Net-S region. However, the P-CNN effectively balances the interplay between dispersion and nonlinear effects through optimized phase selection in the pulse shaper.

First, we demonstrate the optimization of soliton pulses with variable bandwidth. To achieve this, the P-CNN is trained. The target bandwidth is linearly set from 10 to 70 nm, depicted by the blue line in Fig. 4(a), while the optimized measurement outcomes are represented as orange dots. The results reveal prominent agreement between the measurements and the set targets, highlighting the system's ability for precise and continuous tuning of the output's spectral bandwidth.

Next, we explore the feasibility of generation of high-order solitons within the current setup. High-order solitons are a cornerstone of nonlinear optics, characterized by their unique dynamics during propagation. To define the target function, we initiate the pulse as a high-order soliton: $A(t) = N \text{sech}(t)$, and then simulate its dynamics during propagation using the NLSE. During propagation along z , spectro-temporal breather phenomena arise due to the imbalance between the dispersion and SPM for such high-order soliton. The soliton period z_0 , which dictates the propagation length, is evaluated by:

$$z_0 = \frac{\pi}{2} L_d, \quad (6)$$

where $L_d = T_0^2/|\beta_2|$ is the dispersion length. Specifically, the spectral evolution of a third-order soliton ($N = 3$) over one soliton period is illustrated in Fig. 4(b). In the time domain, the soliton contracts to a fraction of its initial width, splits into two pulses at $z_0/2$, and then recombines to its original form at $z = z_0$. This breathing pattern recurs over successive propagation segments z . Practically, capturing the breather pattern would require physically cutting the fiber, an irreversible and labor-intensive process. The P-CNN framework offers more efficient method to search and output all the waveform over one soliton distance at the same one position z , and thus observations of the breather patterns for high-order soliton.

We first set the target spectral pattern to waveform of third-order soliton and used the trained Net-S network alongside a strategic search approach to identify the optimal solution. The measured spectra, shown in the bottom panel of Fig. 4(b), exhibit a high degree of similarity to the target. Consistent with the simulations, the spectral intensity maintains its original profile initially, broadens around $z_0/5$, and reconverges near $z_0/4$. At the midpoint, $z_0/2$, the spectrum splits, displaying conjugate dynamics for the latter half of the propagation from $z_0/2$ to z_0 .

To visualize their dynamics in the temporal domain, we used the FROG system, with results presented in Fig. 4(e). The initial soliton has a pulse duration of approximately 850 fs, which narrows to a minimum of 23 fs at $15/60z_0$, corresponding to a nonlinear compression factor of about 36. As the propagation continues, the pulse broadens and splits at $z_0/2$, closely aligning with simulation results.

The same approach was applied to a fourth-order soliton, with results displayed in Fig. 4(c) and (f), respectively. In this case, the initial pulse duration, approximately 720 fs, reduces to a minimum of 22 fs, corresponding to a nonlinear compression factor of around 33. The temporal evolution of the fourth-order soliton is more complex,

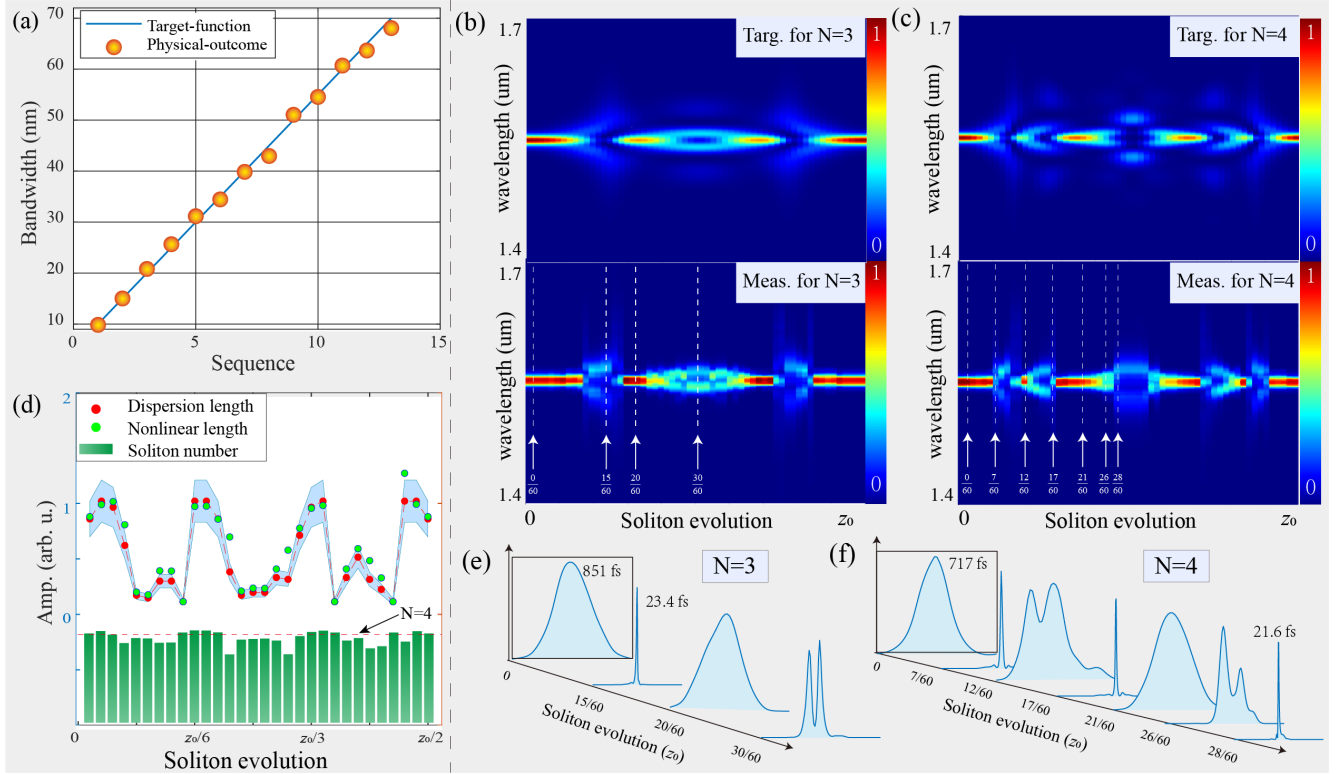


Figure 4. Spectro-temporal correlations for high-order soliton formation. (a) Bandwidth (3dB) of target functions (P-CNN) and measurements, ranging from 10 to 70 nm. (b)-(c) Spectra of high-order solitons for soliton numbers $N=3$ and $N=4$, with the top panels showing simulated target states and the bottom panels presenting experimental measurements. (d) Dispersion length, nonlinear length, and soliton number for a soliton with $N=4$. (e)-(f) Temporal intensity profiles reconstructed via FROG for various soliton sequences.

featuring multiple points of narrow pulse duration, consistent with its intricate spectro-temporal structure. (**Refer to the support flash for additional FROG results on high-order solitons**).

A fundamental model can elucidate the observed dynamics in high-order soliton generation. By analyzing the optimized spectral phase of the initial pulse, reconstructed using a FROG system, we derived the temporal intensity and extracted key parameters, including pulse duration (T_0) and peak power (P_k). From these, we calculated the dispersion length ($L_d = T_0^2 / |\beta_2|$) and nonlinear length ($L_n = 1 / (\gamma P_k)$). These parameters define the soliton number:

$$N^2 = \frac{L_d}{L_n} \approx T_0^2 P_k. \quad (7)$$

Maintaining a consistent soliton number for each sequence is critical for accurately reproducing high-order soliton profiles at the fiber output. Any deviation can destabilize soliton dynamics^{2,47}. Experimentally, adjusting T_0 to modify the dispersion length L_d affects the peak power P_k and, consequently, L_n , potentially disrupting soliton number stability. However, our control over the pulse amplitude (via EDFA gain) and pulse duration (via the pulse shaper) mitigates this issue.

Experimentally, adjusting T_0 to modify the dispersion length L_d can lead to various outputs at the fiber's end. However, such adjustments in T_0 also alter the peak power P_k and, consequently, the nonlinear length L_n , potentially disrupting the conditions necessary for stable soliton number. The ability of PCNN can control both T_0 and P_k , effectively circumvents this issue. Figure 4(d) presents the measured values of L_d (red dots) and L_n (green dots) for $N=4$, demonstrating a periodic behavior. Notably, the soliton number (green bars) remains nearly constant, around 4,

throughout the process, underscoring the importance of soliton number conservation for stable dynamics. **Further theoretical analysis on high-order solitons is provided in Supplementary-3.**

Fig. 4(d) presents the calculated L_d (red dots) and L_n (green dots) based on the measurements for $N=4$ in the pulse duration and peak power, demonstrating a periodic tendency. Remarkably, the soliton number (green bars) remains nearly constant, ~ 4 , throughout the process, underscoring the soliton number conservation over the total dynamics. **(Further theoretical analysis on high-order solitons is provided in Supplementary-3).**

Discussion

In this work, we introduced a physics-trained deep learning framework based on a convolutional neural network, termed P-CNN, designed for flexible spectro-temporal engineering of photonic wavepackets. Unlike the physics-informed neural networks (PINNs) developed in recent years, which are effective for solving partial differential equations (PDEs) and self-learning machines^{48,49}, our approach incorporates the physical representation directly into the input layer rather than the loss function. This distinction allows for a more intrinsic integration of physics-based constraints into the network.

This framework was implemented using an active pulse shaper paired with a nonlinear broadening section consisting of an EDFA and a highly nonlinear fiber assembly. Output pulse characterization via SH-FROG enabled wavepacket-based training of the P-CNN. As shown in simulations, training of CNN on physics-based information (encapsulated in Wigner-function images derived from FROG analysis) provided a threefold improvement in solution determinism compared to brute-force strategies.

We showcased several practical demonstrations of this framework's effectiveness. By analyzing the generated supercontinuum over two distinct networks, Net-D and Net-S, we successfully modeled the behaviors of dispersive waves (DW) and soliton waves (SW), respectively. For Net-D, we demonstrated fine control over DW properties, including center frequency, bandwidth, and pulse duration. Notably, we achieved a minimum infrared pulse duration of 12 fs, corresponding to three optical cycles and near-transform-limited duration. This corresponds to an impressive compression factor of 71, starting from the initial pulse duration of 850 fs. This was accomplished without external pulse compressors, thanks to the P-CNN's ability to balance nonlinear broadening and pulse compression using a single pulse shaper system. Regarding Net-S, we demonstrated on-demand generation of high-order solitons ($N = 3, 4$), capturing characteristic breather dynamics in the spectro-temporal domain as predicted by the nonlinear Schrödinger equation.

These demonstrations highlight the remarkable capabilities of P-CNN-enabled pulse manipulation across both spectral and temporal domains. Conventionally, pulse shaping targets the entire spectral bandwidth of the wavepacket. Here, we extended this shaping to ultrabroadband contexts, achieving a spectral coverage expansion by 12-fold than the bandwidth of the linear pulse shaper. This underscores the compactness and efficiency of the proposed spectro-temporal shaping strategy.

An intriguing extension of this work lies in combining spectro-temporal (ω, t) engineering with spatial degrees of freedom (k, x) , paving the way for full space-time designer wavepackets⁵⁰⁻⁵². In addition, this approach can be generalized to manipulate wavepackets in multidimensional correlation spaces, such as (ω, k) or (t, x) , offering new possibilities for nonlinear interactions and advanced beam shaping.

Beyond the demonstrations presented, we believe the P-CNN framework can be applied to engineer arbitrary photonic states, particularly those arising from highly nonlinear optical interactions governed by the GNLSE. Furthermore, this method shows promise as an effective machine learning tool for solving other PDEs, which are fundamental to describing natural physical laws⁵³. Finally, the approach holds promises in accelerating optical computations in fields such as AI photonics, neuromorphic systems, and quantum optical computing^{38,54,55}.

Acknowledgements

The authors would like to thank Prof. Ebrahim Karimi's SQO group for providing the spatial light modulator. We appreciate following colleagues in Polytechnique Montréal for kind help during experiments and fruitful discussions: Mr. Mikaél Leduc, Dr. Sho Onoe, Mr. Laurent Rivard, Mr. Marco Scaglia, Mr. Émile Dessureault, Mr. Grégory-Samuel Zagbayou, Mr. Rodrigo Itzamna Becerra Deana, as well as Mr. Émile Jetzer. We thank Mrs. Christine Tao (Temo. Optics Inc.) for improvements in figure aesthetics.

This work was funded by Natural Sciences and Engineering Research Council of Canada (NSERC), via the Canada Research Chair program (CRC), and Fonds de Recherche du Québec–Nature et Technologies (FRQNT), via Institut Transdisciplinaire d'Information Quantique (INTRIQ), and by the European Union's Horizon Europe Research and Innovation Programme under agreement 101070700 (project MIRAQLS). S.L. acknowledges the support PBE/EE/Bourses de court séjour de recherche ou perfectionnement, FRONT of Canada and Mitacs Accelerate Program.

References

1. Ranka, J. K., Windeler, R. S. & Stentz, A. J. Visible continuum generation in air–silica microstructure optical fibers with anomalous dispersion at 800 nm. *Opt. Lett.* **25**, 25–27, DOI: [10.1364/OL.25.000025](https://doi.org/10.1364/OL.25.000025) (2000).
2. Agrawal, G. P. Nonlinear fiber optics. In *Nonlinear Science at the Dawn of the 21st Century*, 195–211 (Springer, 2000).
3. Alfano, R. R. *The supercontinuum laser source: fundamentals with updated references* (Springer, 2006).
4. Dudley, J. M., Genty, G. & Coen, S. Supercontinuum generation in photonic crystal fiber. *Rev. modern physics* **78**, 1135 (2006).
5. Sell, A., Krauss, G., Scheu, R., Huber, R. & Leitenstorfer, A. 8-fs pulses from a compact er: fiber system: quantitative modeling and experimental implementation. *Opt. Express* **17**, 1070–1077, DOI: [10.1364/OE.17.001070](https://doi.org/10.1364/OE.17.001070) (2009).
6. Borondics, F. *et al.* Supercontinuum-based fourier transform infrared spectromicroscopy. *Optica* **5**, 378–381 (2018).
7. Kaminski, C., Watt, R., Elder, A., Frank, J. & Hult, J. Supercontinuum radiation for applications in chemical sensing and microscopy. *Appl. Phys. B* **92**, 367–378 (2008).
8. Gündoğdu, S., Virally, S., Scaglia, M., Seletskiy, D. V. & Moskalenko, A. S. Self-referenced subcycle metrology of quantum fields. *Laser & Photonics Rev.* **17**, 2200706 (2023).
9. Tu, H. & Boppart, S. A. Coherent fiber supercontinuum for biophotonics. *Laser & photonics reviews* **7**, 628–645 (2013).
10. Ji, X. *et al.* Millimeter-scale chip-based supercontinuum generation for optical coherence tomography. *Sci. Adv.* **7**, eabg8869 (2021).
11. Jones, D. J. *et al.* Carrier-envelope phase control of femtosecond mode-locked lasers and direct optical frequency synthesis. *Science* **288**, 635–639, DOI: [10.1126/science.288.5466.635](https://doi.org/10.1126/science.288.5466.635) (2000). <https://www.science.org/doi/pdf/10.1126/science.288.5466.635>.
12. Sinclair, L. C. *et al.* Invited article: A compact optically coherent fiber frequency comb. *Rev. Sci. Instrum.* **86**, 081301 (2015).
13. Fehrenbacher, D. *et al.* Free-running performance and full control of a passively phase-stable er: fiber frequency comb. *Optica* **2**, 917–923, DOI: [10.1364/OPTICA.2.000917](https://doi.org/10.1364/OPTICA.2.000917) (2015).
14. Krauss, G. *et al.* Synthesis of a single cycle of light with compact erbium-doped fibre technology. *Nat. Photonics* **4**, 33–36 (2010).

15. Shumakova, V. *et al.* Multi-millijoule few-cycle mid-infrared pulses through nonlinear self-compression in bulk. *Nat. communications* **7**, 12877 (2016).
16. Steinleitner, P. *et al.* Single-cycle infrared waveform control. *Nat. Photonics* **16**, 512–518 (2022).
17. Peng, P., Marceau, C. & Villeneuve, D. M. Attosecond imaging of molecules using high harmonic spectroscopy. *Nat. Rev. Phys.* **1**, 144–155 (2019).
18. Li, J. *et al.* Attosecond science based on high harmonic generation from gases and solids. *Nat. Commun.* **11**, 2748 (2020).
19. Brès, C.-S. *et al.* Supercontinuum in integrated photonics: generation, applications, challenges, and perspectives. *Nanophotonics* **12**, 1199–1244 (2023).
20. Beetar, J. E. *et al.* Multioctave supercontinuum generation and frequency conversion based on rotational nonlinearity. *Sci. Adv.* **6**, eabb5375 (2020).
21. Elu, U. *et al.* Seven-octave high-brightness and carrier-envelope-phase-stable light source. *Nat. Photonics* **15**, 277–280 (2021).
22. Piccoli, R. *et al.* Intense few-cycle visible pulses directly generated via nonlinear fibre mode mixing. *Nat. Photonics* **15**, 884–889 (2021).
23. Genty, G., Coen, S. & Dudley, J. M. Fiber supercontinuum sources. *JOSA B* **24**, 1771–1785 (2007).
24. Genier, E. *et al.* Ultra-flat, low-noise, and linearly polarized fiber supercontinuum source covering 670–1390 nm. *Opt. Lett.* **46**, 1820–1823 (2021).
25. Wetzell, B. *et al.* Customizing supercontinuum generation via on-chip adaptive temporal pulse-splitting. *Nat. communications* **9**, 4884 (2018).
26. Sylvestre, T. *et al.* Recent advances in supercontinuum generation in specialty optical fibers. *JOSA B* **38**, F90–F103 (2021).
27. Tzang, O., Caravaca-Aguirre, A. M., Wagner, K. & Piestun, R. Adaptive wavefront shaping for controlling nonlinear multimode interactions in optical fibres. *Nat. Photonics* **12**, 368–374 (2018).
28. Hary, M. *et al.* Tailored supercontinuum generation using genetic algorithm optimized fourier domain pulse shaping. *Opt. Lett.* **48**, 4512–4515 (2023).
29. Lapre, C. *et al.* Genetic algorithm optimization of broadband operation in a noise-like pulse fiber laser. *Sci. Reports* **13**, 1865 (2023).
30. Martins, G. R., Silva, L. C., Segatto, M. E., Rocha, H. R. & Castellani, C. E. Design and analysis of recurrent neural networks for ultrafast optical pulse nonlinear propagation. *Opt. Lett.* **47**, 5489–5492 (2022).
31. Hoang, V. T. *et al.* Optimizing supercontinuum spectro-temporal properties by leveraging machine learning towards multi-photon microscopy. *Front. Photonics* **3**, 940902 (2022).
32. Shih, M. *et al.* Maximizing supercontinuum bandwidths in gas-filled hollow-core fibers using artificial neural networks. *J. Appl. Phys.* **133** (2023).
33. Farfan, C. A., Epstein, J. & Turner, D. B. Femtosecond pulse compression using a neural-network algorithm. *Opt. Lett.* **43**, 5166–5169 (2018).
34. Boscolo, S. & Finot, C. Artificial neural networks for nonlinear pulse shaping in optical fibers. *Opt. & Laser Technol.* **131**, 106439 (2020).
35. Salmela, L. *et al.* Feed-forward neural network as nonlinear dynamics integrator for supercontinuum generation. *Opt. Lett.* **47**, 802–805 (2022).
36. Närhi, M. *et al.* Machine learning analysis of extreme events in optical fibre modulation instability. *Nat. communications* **9**, 4923 (2018).

37. Salmela, L., Lapre, C., Dudley, J. M. & Genty, G. Machine learning analysis of rogue solitons in supercontinuum generation. *Sci. Reports* **10**, 9596 (2020).
38. Genty, G. *et al.* Machine learning and applications in ultrafast photonics. *Nat. Photonics* **15**, 91–101 (2021).
39. Zuo, C. *et al.* Deep learning in optical metrology: a review. *Light. Sci. & Appl.* **11**, 39 (2022).
40. Malomed, B. A. Optical solitons and vortices in fractional media: A mini-review of recent results. In *Photonics*, vol. 8, 353 (Multidisciplinary Digital Publishing Institute, 2021).
41. Liu, S., Zhang, Y., Malomed, B. A. & Karimi, E. Experimental realisations of the fractional schrödinger equation in the temporal domain. *Nat. Commun.* **14**, 222 (2023).
42. McKay, M. D., Beckman, R. J. & Conover, W. J. A comparison of three methods for selecting values of input variables in the analysis of output from a computer code. *Technometrics* **42**, 55–61 (2000).
43. Walmsley, I. A. & Dorrer, C. Characterization of ultrashort electromagnetic pulses. *Adv. Opt. Photonics* **1**, 308–437 (2009).
44. Köttig, F. *et al.* Mid-infrared dispersive wave generation in gas-filled photonic crystal fibre by transient ionization-driven changes in dispersion. *Nat. communications* **8**, 813 (2017).
45. Moussa, H. *et al.* Observation of temporal reflection and broadband frequency translation at photonic time interfaces. *Nat. Phys.* **19**, 863–868 (2023).
46. Anderson, D. & Lisak, M. Nonlinear asymmetric self-phase modulation and self-steepening of pulses in long optical waveguides. *Phys. Rev. A* **27**, 1393 (1983).
47. Malomed, B. A. *Soliton management in periodic systems* (Springer Science & Business Media, 2006).
48. Karniadakis, G. E. *et al.* Physics-informed machine learning. *Nat. Rev. Phys.* **3**, 422–440 (2021).
49. Lopez-Pastor, V. & Marquardt, F. Self-learning machines based on hamiltonian echo backpropagation. *Phys. Rev. X* **13**, 031020 (2023).
50. Jolly, S. W., Gobert, O. & Quéré, F. Spatio-temporal characterization of ultrashort laser beams: a tutorial. *J. Opt.* **22**, 103501, DOI: [10.1088/2040-8986/abad08](https://doi.org/10.1088/2040-8986/abad08) (2020).
51. Korman, S., Bahar, E., Arieli, U. & Suchowski, H. Spatio-temporal ultrafast pulse shaping at the femtosecond–nanometer scale. *Opt. Lett.* **47**, 4279–4282, DOI: [10.1364/OL.461953](https://doi.org/10.1364/OL.461953) (2022).
52. Chong, A., Wan, C., Chen, J. & Zhan, Q. Generation of spatiotemporal optical vortices with controllable transverse orbital angular momentum. *Nat. Photonics* **14**, 350–354 (2020).
53. Brunton, S. L. & Kutz, J. N. Promising directions of machine learning for partial differential equations. *Nat. Comput. Sci.* 1–12 (2024).
54. McMahon, P. L. The physics of optical computing. *Nat. Rev. Phys.* **5**, 717–734 (2023).
55. Fischer, B. *et al.* Neuromorphic computing via fission-based broadband frequency generation. *Adv. Sci.* **10**, 2303835 (2023).